Bismuth mobile promoter and cobalt-bismuth nanoparticles in carbon nanotube supported Fischer-Tropsch catalysts with enhanced stability

Bang Gu[a†], Deizi V. Peron[a], Alan J. Barrios[a,b], Mirella Virginie[a], Camille La Fontaine[c], Valérie Briois[c], Mykhailo Vorokhta[d], Břetislav Šmíd[d], Simona Moldovan[e], Siddardha Koneti[e], Thobani G. Gambu[b], Mark Saeys[b], Vitaly V. Ordomsky[a] and Andrei Y. Khodakov[a*]*

[a]*Univ. Lille, CNRS, Centrale Lille, Univ. Artois, UMR 8181 – UCCS – Unité de Catalyse et Chimie du Solide, F-59000 Lille, France*

[b]*Laboratory for Chemical Technology (LCT), Department of Materials, Textiles and Chemical Engineering, Ghent University, Technologiepark 125, 9052 Ghent, Belgium*

[c]*Synchrotron SOLEIL, L'Orme des Merisiers - St. Aubin, BP 48, 91192, Gif-sur-Yvette Cedex, France*

[d]*Department of Surface and Plasma Science, Faculty of Mathematics and Physics, Charles University, V Holešovičkách 747/2, 180 00 Praha 8, Czechia*

[e]*Groupe de Physique des Matériaux, CNRS, Université Normandie & INSA Rouen Avenue de l'Université - BP12, 76801 St Etienne du Rouvray, France*

**Corresponding authors*

[†]*Present address:* School of Chemical Science and Technology, Key Laboratory of Medicinal Chemistry for Natural Resource-Ministry of Education, Functional Molecules Analysis and Biotransformation Key Laboratory of Universities in Yunnan Province, Advanced Analysis and Measurement Center, Yunnan University, 2 North Cuihu Road, 650091 Kunming, China

Abstract

Metal nanoparticles on the surface of porous supports have found numerous applications in different areas of science. Fischer-Tropsch synthesis, which proceeds on the surface of cobalt metal nanoparticles, is an efficient way to convert renewables and fossil feedstocks into alternative fuels. The stability of cobalt catalysts is an essential and even crucial parameter and can be significantly improved by promotion.

In this paper, a combination of *operando* Quick-XAS, NAP-XPS, high resolution electron microscopy imaging, DFT modeling alongside with Fischer-Tropsch catalytic experiments has provided deep insights into the evolution of bismuth promoter and structure of cobalt-bismuth nanoparticles in the catalysts supported by carbon nanotubes. We uncovered noticeable migration of metallic bismuth occurring during the reduction step, which leads to bismuth redispersion over the surface of cobalt nanoparticles. Cobalt reduction is facilitated in the presence of bismuth. The working Fischer-Tropsch catalyst contains cobalt-bismuth bimetallic nanoparticles, with bismuth located in the nanoparticle shell. The promotion with bismuth has resulted in a noticeable increase in catalyst stability. Characterization and DFT modelling suggest preferential localization of bismuth mobile promoter at the steps and edges of cobalt nanoparticles, which hinders cobalt sintering and carbon deposition and improves the catalyst stability.

Keywords: operando; catalysis; liquid metals; bismuth; cobalt; stability; Fischer-Tropsch

Introduction

Metal nanoparticles have found numerous applications in different areas of chemistry, physics, materials science and medicine [1,2]. Small metal nanoparticles are thermodynamically non-stable, because of their higher surface energy. Synthesis of metal nanoparticles with the desired size and shape and enhanced stability is an important challenge [3,4], which requires interdisciplinary knowledge and strategies.

Fischer-Tropsch (FT) synthesis is an efficient technology for syngas (H_2 and CO mixture) conversion into valuable fuels and chemicals [5,6]. Cobalt catalysts are the catalysts of choice [5–8] for low temperature FT synthesis, which takes place with syngas pressure of 20-40 bar, at temperature of 220-240 ^{o}C and stoichiometric H_2/CO ratio of 2. FT synthesis occurs over small cobalt metal nanoparticles localized over porous oxide or carbon supports [8]. Prior to the FT reaction, cobalt catalysts require reduction of cobalt oxide species to metallic nanoparticles.

Metals and metal alloys with low melting points are a new class of materials, which have gained growing attention in many fields including microfluidics, flexible electronics and drug delivery [9,10]. Recently, we discovered [11–14] strong promoting effects of bismuth on the catalytic performance of iron, cobalt and nickel catalysts in carbon monoxide hydrogenation. We found [12] that the bismuth promoter could increase up to 10 times the activity of iron catalysts in high temperature FT synthesis. Bismuth also enhances the catalyst stability due to hindering both metal nanoparticle sintering and carbon deposition [11]. The enhancement of stability after Bi promotion was particularly pronounced [11] for silica-supported cobalt catalysts. The reduced carbon deposition and sintering were respectively attributed [11] to the bismuth oxidation−reduction cycling during carbon monoxide hydrogenation. The melting point of metallic bismuth is 271 °C. This gives for this metal very low Tamman and Hüttig temperatures [15]. The Hüttig temperature is relevant to the mobility of defects, while the Tamman temperature is relevant to the mobility of bulk atoms. Therefore, bismuth is expected to present high mobility at the temperature of catalyst activation and FT reaction.

The present work addresses in-depth investigation of the interaction of cobalt and bismuth in the carbon nanotube (CNT) supported catalysts, which have demonstrated enhanced stability in low temperature FT synthesis. The detailed information about the evolution of cobalt and bismuth species in the CNT supported catalysts during the catalyst activation, FT reaction and passivation was extracted from a combination of *operando* Quick X-ray Absorption Spectroscopy *(Quick-XAS)* operating during FT reaction at the realistic operational conditions, surface-sensitive Near Ambient Pressure X-ray Photoelectron Spectroscopy (NAP-XPS), Density Functional Theory (DFT) modeling and Transmission Electron Microscopy (TEM). The characterization results are discussed alongside with the FT catalytic performance and catalyst stability data.

Experimental

Preparation of catalysts

Carbon nanotubes (CNT) with an outer diameter of 20-40 nm were purchased from IoLiTec Nanomaterials. The raw CNTs were treated with a 68 wt.% nitric acid at 140

^{o}C for 14 h, followed by washing and drying in order to remove impurities and to oxidize the CNT surface. The procedure is described in detail in our previous reports [13,16]. The CNT-supported cobalt catalysts were prepared by the conventional incipient wetness impregnation. Cobalt nitrate ($Co(NO_3)_2.6H_2O$, Sigma-Aldrich) and bismuth nitrate ($Bi(NO_3)_3.5H_2O$, Sigma-Aldrich) were used as cobalt and bismuth precursors, respectively. The Co and Bi contents in the catalysts were fixed at 15 wt.% and 0.2 wt.%, respectively. For the NAP-XPS and STEM-EDX experiments, the Bi content in the catalysts was set to 2 wt. %. After the impregnation, the obtained powdery catalysts were further dried at 80 ^{o}C for 12 h and calcined in nitrogen at 400 ^{o}C for 4 h. The Bi/CNT (10 wt.% Bi) sample was also prepared by the same synthesis procedure. The Bi-promoted cobalt catalyst was also prepared by mechanical mixing following the procedure from our previous report [13]. The Co/CNT and Bi/CNT samples were mechanically mixed in an agate mortar for 10 min to obtain the catalysts with the same cobalt and bismuth contents as in the co-impregnated counterparts. The obtained physical mixture catalyst was denoted as Co/CNT+Bi/CNT.

Catalyst characterization

The X-ray diffraction (XRD) patterns were recorded on a PANalytical Empyrean X-ray diffractometer. The Cu Kα radiation (40 kV and 30 mA) was used as the X-ray source. Low-temperature N_2 adsorption-desorption was performed on a Micromeritics Tristar Model 3020 Surface Area and Porosimetry analyzer. Prior to the N_2 adsorption, the samples were degassed under vacuum at 250 ^{o}C for 2 h. The metal contents were measured by inductively coupled plasma-optic emission 720-ES ICP-OES spectroscopy (Agilent). The H_2 temperature-programmed reduction (H_2-TPR, 5% H_2 in Ar) was carried out using the AutoChem II 2920 apparatus (Micromeritics). The temperature was increased from 50 ºC to 800 ºC with the heating rate of 10 ºC min^{-1}.

The Co K edge and Bi L_3 edge Quick X-ray absorption spectra (Quick-XAS) were obtained *in situ* in the transmission mode during the catalyst reduction under hydrogen, air passivation and FT reaction under syngas on the ROCK beamline of the SOLEIL synchrotron (Gif-sur-Yvette, France) [17] with a time resolution of 250 ms per spectrum. The Si(111) channel-cut crystal was used for acquisitions at both edges. The quartz capillary reactor (OD=1 mm, wall thickness=0.020 mm) was used for *in-situ* Quick-XAS measurements with the catalyst loading of 3-5 mg. The capillary was attached to the stainless-steel holder using a high temperature epoxy glue. The reactor temperature was controlled by an OXFORD-FMB gas blower, while the total pressure in the reactor (up to 10 bar) was regulated by a back-pressure controller. For monitoring of the treatment of the Bi-promoted CoBi/CNT catalyst, Quick-XAS measurements were carried out at both edges on the same samples using the "edge jumping" capability offered at the ROCK beamline [18]. In that case, the measurements at the Co K edge for 25 s were performed alternately with measurements at the Bi L_3 edge for 55 s, with elapsed time of about 70 s between each edge alternation required for moving harmonic rejection mirror stripes and Bragg angles of the Si(111) channel-cut suitable for each edge. The longer acquisition time for Bi L_3 edge than for the Co ones was due to the small Bi edge jump measured in transmission mode, which was around 0.035 compared to 2.0 at the Co K edge. In order to improve the S/N ratio, 110 spectra recorded in 250 ms were merged at the Bi L_3

edge against 50 spectra at the Co K edge. Normalization and energy calibration of the data were performed using the Python interface developed at the ROCK beamline [17,19]. Cobalt and bismuth speciations were obtained thanks to the multivariate curve regression with alternating least-square (MCR-ALS) analysis [20] using the MCR-ALS 2.0 Matlab toolbox developed by Tauler's group [21]. This method, which has been described in details for time-resolved Quick-XAS data in references [19,22,23] permits to isolate from the data set the spectra of each pure species participating to the reaction and its concentration profile. The outcome files obtained using the MCR-ALS 2.0 Matlab toolbox for the different catalysts are given in **Supplementary Material** (**SM**). The EXAFS analysis at the Bi L_3 edge of the catalysts after reduction and air passivation was performed using the Athena and Artemis software [24]. The reaction products were monitored by Raman Spectroscopy using a 532 nm KAISER Raman spectrometer equipped with a probe head located at the outlet of the capillary reactor [25].

The Scanning Transmission Electron Microscopy (STEM) analyses were carried on a double corrected analytical JEOL TEM 200 CF operated at 200 kV. The elemental maps acquisitions (256 x 256 pixels) were carried out using the Energy Dispersive X-ray Spectrometer (EDX) Centurio 100 detector with a scanning speed of 0.05 ms/px, whilst applying a drift correction every 60 seconds. STEM micrographs were acquired using a High Angular Annular Dark Field (HAADF) detector with a camera length of 8 cm and a spot diameter of 0.1 nm.

NAP-XPS was performed in Prague using a spectrometer custom-built by SPECS Surface Nano Analysis, GmbH Germany. An ultrahigh vacuum (UHV) system equipped with a PHOIBOS 150 Hemispheric Energy Analyser and an Al Kα monochromatized X-ray source of high intensity (excitation energy of 1486.6 eV) was employed to perform X-ray Photoelectron Spectroscopy (XPS) measurements [26]. The *in-situ* reaction cell was set in the analysis chamber allowing XPS measurements in the presence of gases with pressure up to 10 mbar and at high temperature. Typically, the catalyst (~20 mg) was pressed into a tungsten mesh together with a K-type thermocouple and spot welded to a stainless-steel sample holder. The measurements were performed in presence of H_2 or syngas (1 mbar) at the temperature ranging from ambient to 315 ºC. The XPS spectra were analyzed by fitting the Shirley-type function with the Casa XPS software. In order to visualize clearly the localization of the promoter, TEM and NAP-XPS experiments were performed with the model CoBi/CNT catalysts containing 2 wt.% Bi.

Operando and laboratory catalytic tests

The FT reaction over the CNT-supported cobalt catalysts was performed both in the quartz capillary *operando* reactor (d_{in}=0.8 mm) at the ROCK beamline of the Soleil synchrotron and in the laboratory tubular stainless-steel fixed bed reactor (d_{in}=8 mm). For the synchrotron *operando* experiments, the capillary reactor was set in sequence with a pre-bed reactor filled with the same catalyst and heated at the same temperature, in order to expose the catalyst to high conversion levels. 100 mg catalyst was loaded in the pre-bed reactor and 3-5 mg catalyst was added to the capillary reactor, respectively. The catalyst activation, passivation and FT reaction were conducted simultaneously with *operando* Quick-XAS measurements.

The same cobalt catalysts were also tested in the laboratory made fixed-bed reactor. The following conditions were typically used: P=20 bar, H_2/CO=2 and GHSV=6.3 L/g.h. N_2 was used as internal standard. The products of FT synthesis in both capillary and laboratory FT reactors were analyzed using a gas chromatograph (Scion GC-450). A thermal conductivity detector (TCD), equipped with a CTR-1 column, was used to analyze N_2, CO, CO_2 and CH_4. A flame ionization detector (FID) was used for analysis of hydrocarbons separated on a Rt-Q-PLOT capillary column. The liquid products (oil and water phases) were collected in a trap kept at 80 °C and analyzed off-line by gas chromatography. The product selectivity was calculated on carbon basis without considering CO_2. The carbon balances were all better than 90 %. The selectivity to CO_2 was calculated separately.

Computational Methods

Spin-polarized periodic density functional theory (DFT) calculations were performed using the vdW-DF2 functional [27,28], as implemented in the Vienna *ab initio* simulation package (VASP) [29,30], together with a projector augmented wave (PAW) method. A plane wave kinetic energy cutoff of 450 eV was found to be sufficiently converged. The electronic structure was optimized to within 10^{-5} eV. The 2nd order Mathfessel-Paxton (MP) method with a smearing width of 0.2 was used. The Co(111), Co(100) and Co(211) surfaces were modeled as six-, five- and four-layered slabs cleaved from optimized bulk fcc-cobalt, respectively. For the Co(111) and Co(100) slabs, only the top three layers were allowed to fully relax during geometry optimization, whilst for the Co(211), only the top two layers were relaxed. For all unit cells studied, viz. p(3x3), p(2x3), p(2x4) and p(2√3x2√3)R30°, the Monkhorst-Pack grid was adjusted to give a k-point density of ca. 0.038 Å^{-1} with only a single k-point along the longest lattice vector. Periodic slabs were separated by a vacuum gap of 15 Å. All adsorbates were added only on the relaxed side of the surface and a geometry optimization convergence criterion of 0.01 eV/Å was used.

Bulk bismuth oxide and metallic bismuth were optimized using their respectively optimized k-point grids. Statistical thermodynamics was used to calculate the Gibbs free energies of gas molecules as well as adsorbed species. The substitutional Gibbs free energy was calculated as follows:

$$0.5\ Bi_2O_3 + CO_y/Co(hkl) + (0.5 + y)\ H_2 \rightarrow Bi/Co(hkl) + (0.5 + y)\ H_2O + CO$$

$$\Delta G = G_{Bi/Co(hkl)} + \left(\frac{1}{2} + y\right) G_{H_2O} + G_{CO} - \frac{1}{2} E_{B_2O_3} - G_{CO_y/Co(hkl)} - \left(\frac{1}{2} + y\right) G_{H_2}$$

where the G is the Gibbs free energy and the Bi/Co(hkl), CO$_y$/Co(hkl) subscripts represent adsorbed Bi and CO$_y$, $y \in \{1, 0\}$, on the Co(hkl) surface. $E_{Bi_2O_3}$ is the electronic energy of the bulk bismuth oxide. The Gibbs free energy depends on the partial pressures of CO, H_2 and H_2O as well as temperature.

Results

Ex-situ catalyst characterization

The textural properties of the CNT support and cobalt-based catalysts are displayed in **Table S1, SM**. The CNTs exhibit a high surface area of 145.3 m^2/g. As expected [8], the BET surface area and pore volume decrease after the CNT impregnation with Co or Bi. This is caused by partial pore blocking by cobalt or bismuth species and by the effect of CNT “dilution” with the metals introduced by impregnation. **Table S1, SM** also shows the ICP elemental analysis data. All the three catalysts have similar cobalt content (around 15 wt.%), while the Bi contents were close to 0.2 wt.% in the impregnated and mechanically mixing catalysts. ICP analysis of the spent catalyst showed that the bismuth content remained similar to the catalyst inventory composition (**Table S1, SM**). No bismuth leaching occurred during the reaction.

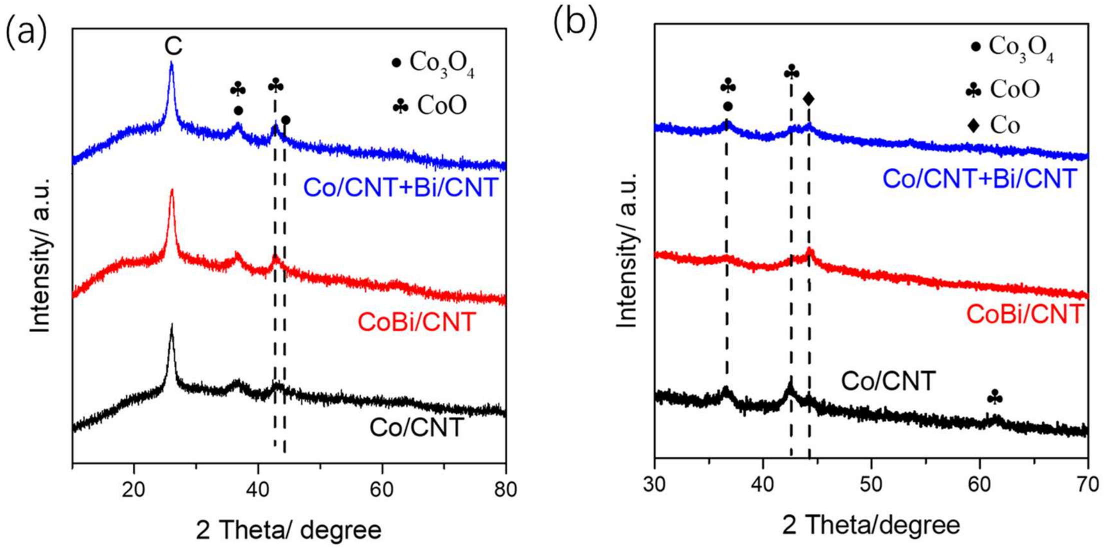

Figure 1. XRD profiles of the freshly calcined catalysts (a) and used catalysts (b) after contact with air for 7 days.

The XRD profiles of the freshly calcined catalysts are presented in **Figure 1a**. They exhibit the diffraction lines attributed to both Co_3O_4 and CoO phases. The presence of CoO is possibly due to the partial reduction of Co_3O_4 by the CNT carbon species during the decomposition of cobalt nitrate. After the introduction of Bi to the cobalt catalysts, the cobalt oxide phase composition in the calcined catalysts remains the same. Calculation of the Co_3O_4 crystallite sizes from the XRD diffraction line broadening yields the values in the range of 9-10 nm (**Table S1, SM**). The XRD patterns of the used catalysts (**Figure 1b**) show the presence of both cobalt oxide and cobalt metallic phases. The diffraction line at 26°, attributed to CNTs, keeps similar a high intensity in the used catalysts.

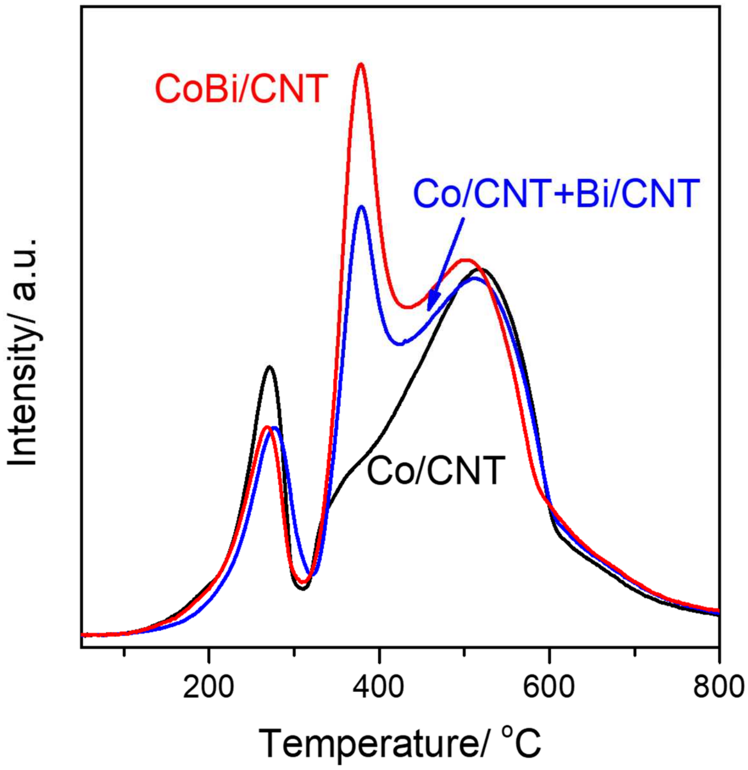

Figure 2. TPR profiles of the freshly calcined CNT-supported cobalt catalysts.

Figure 2 shows the H_2-TPR profiles of the non-promoted Co/CNT and Bi-promoted catalysts. Three main peaks can be observed. The reduction of Co_3O_4 proceeds [31–33] via intermediate formation of CoO, while CoO can be directly reduced to metallic cobalt. The small peak at about 270 °C is therefore, attributed to the reduction of Co_3O_4 to CoO. The second peak, located at about 380 °C, is assigned to the reduction of CoO to metallic Co. The nature of the third peak above 430 °C seems to be more complex. It may be assigned to the reduction of smaller cobalt oxide nanoparticles or gasification of the CNT supports [34–36]. The bismuth promotion results in a higher intensity of the TPR peaks and probably corresponds to a higher extent of cobalt reduction. The total hydrogen consumption during TPR experiments is shown in **Table S1, SM**. The total hydrogen consumption in the catalysts increases in the following order: Co/CNT< Co/CNT+Bi/CNT < CoBi/CNT. The intensity of the peaks at 380 °C significantly increases after the bismuth promotion in the catalysts prepared by impregnation. Even the Co/CNT+Bi/CNT catalyst prepared by mechanical mixing presents the easier reduction ability compared with the Co/CNT catalyst. Better catalyst reducibility can be assigned to the promoting effect of bismuth on cobalt reduction and possibly to the occurrence of cobalt nanoparticles in close interaction with bismuth in the promoted catalysts. Note that the Bi content in the catalysts (0.2 wt.%) was too small to contribute to any noticeable extent to the intensity of the TPR peaks.

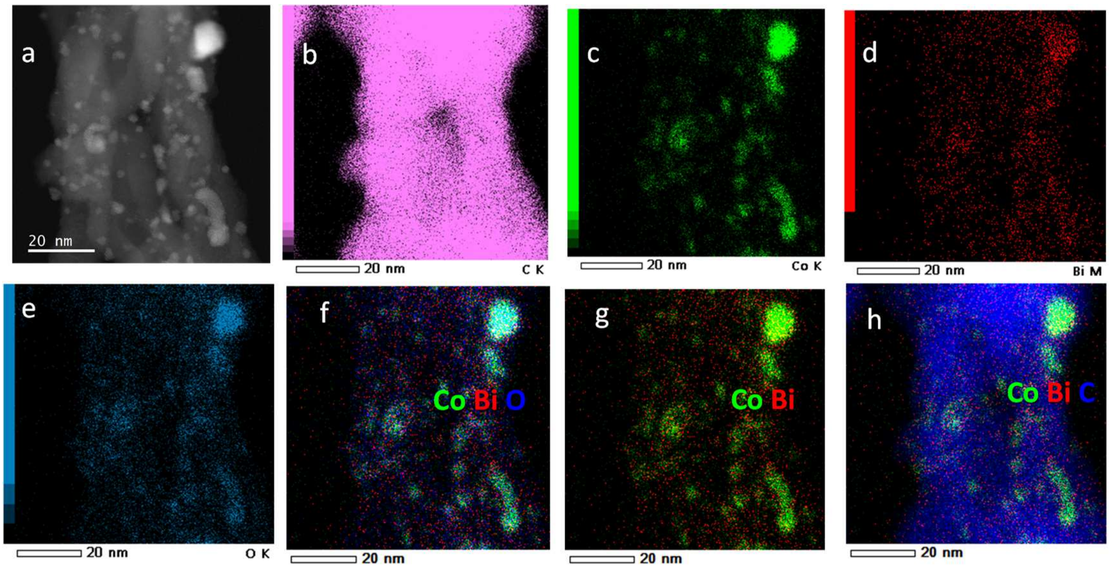

Figure 3. STEM-HAADF micrograph (a) and STEM-EDX elemental maps (b-f) of the freshly calcined CoBi/CNT catalyst (2 wt.% Bi): (b) chemical map of C, (c) chemical map of Co, (d) chemical map of Bi, (e) chemical map of oxygen, (f) superimposed chemical maps of Co, Bi and O, (g) superimposed chemical maps of Co and Bi and (h) superimposed chemical maps of Co Bi and C.

The STEM-HAADF images and STEM-EDX chemical maps of the freshly calcined and activated CoBi/CNT catalysts are shown in **Figures 3, 4, S1-S4, SM**. In freshly calcined CoBi/CNT, larger (>15 nm) and smaller (<5 nm) nanoparticles were detected within the CNTs **(Figure S1, SM**). The small nanoparticles are located on the CNTs surface as well as on the inner CNT tube channels. The Bi atoms were identified within both large and small size cobalt oxide nanoparticles located both in inner channels or outside CNTs (**Figure S2, SM**). The High-Resolution STEM-HAADF observations are consistent with the STEM-EDX (**Figure 3**) findings, which show distinct cobalt nanoparticles and bismuth species localized both on the surface of cobalt oxide nanoparticles and directly on the CNT support.

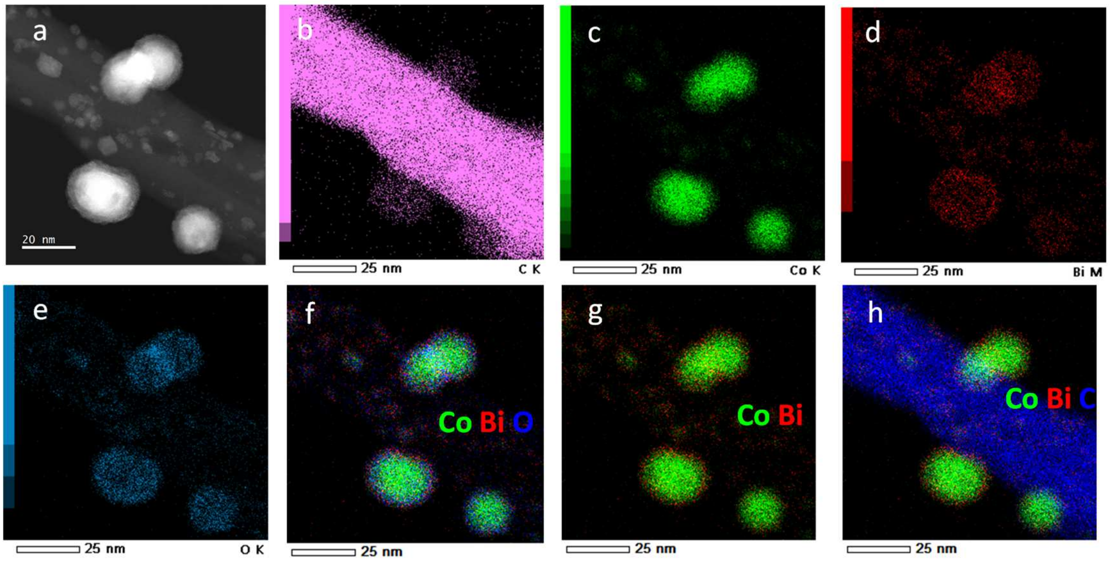

Figure 4. STEM-HAADF micrograph (a) and STEM-EDX elemental maps (b-f) of the activated CoBi/CNT catalyst (2wt.% Bi): (b) chemical map of C, (c) chemical map of Co, (d) chemical map of Bi, (e) chemical map of oxygen, (f) superimposed chemical maps of Co, Bi and O, (g) superimposed chemical maps of Co and Bi and (h) superimposed chemical maps of Co Bi and C.

Similar to the calcined CoBi/CNT catalyst, two populations of nanoparticles are identified (**Figures 4** and **S3, SM**) in activated CoBi/CNT. The larger particles have the sizes larger than 20 nm (up to more than 50 nm), with shapes varying from elongated to rather rounded and morphologies evolving from homogenous (uniform contrast) with the Bi atoms uniformly distributed over the Co nanoparticle surface (**Figure 5**). The shape and morphology of smaller nanoparticles changed from round and regular to facetted. Moreover, the shell of these nanoparticles also contains large amounts of bismuth (higher Z element) (**Figure S4, SM**). The STEM-EDX maps (**Figure 4**) suggest preferential location of the bismuth over the surface of cobalt nanoparticles in particular, in the reduced catalysts. The STEM-EDX map of oxygen (**Figure 4e** and **f**) indicates partial oxidation of metal nanoparticles in the activated catalyst, which is probably caused by the exposure to air during the passivation.

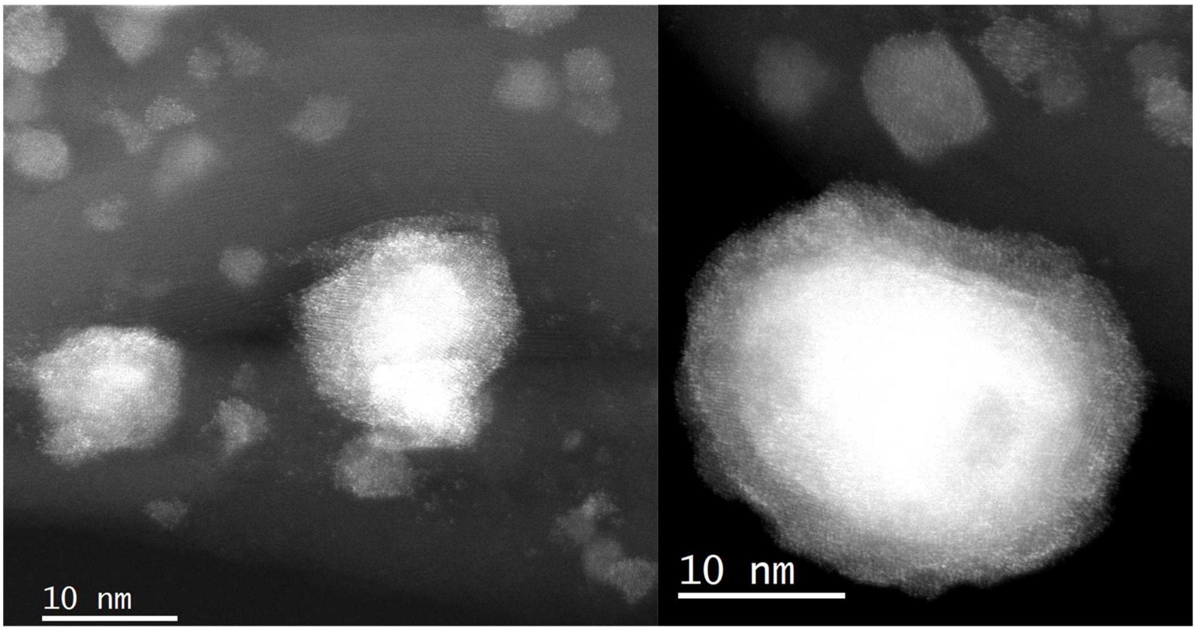

Figure 5. High resolution STEM-HAADF images, showing cobalt-bismuth core-shell nanoparticles in the activated CoBi/CNT catalyst (2 wt.% Bi).

Catalytic performance in the laboratory fixed-bed reactor

The catalytic performance of the monometallic Co/CNT, Bi-promoted cobalt CoBi /CNT and Co/CNT+Bi/CNT catalysts prepared by either impregnation or mechanical mixing method was tested in the laboratory fixed-bed reactor (**Table 1, Figure 6**) at H_2/CO=2 and 20 bar of total pressure.

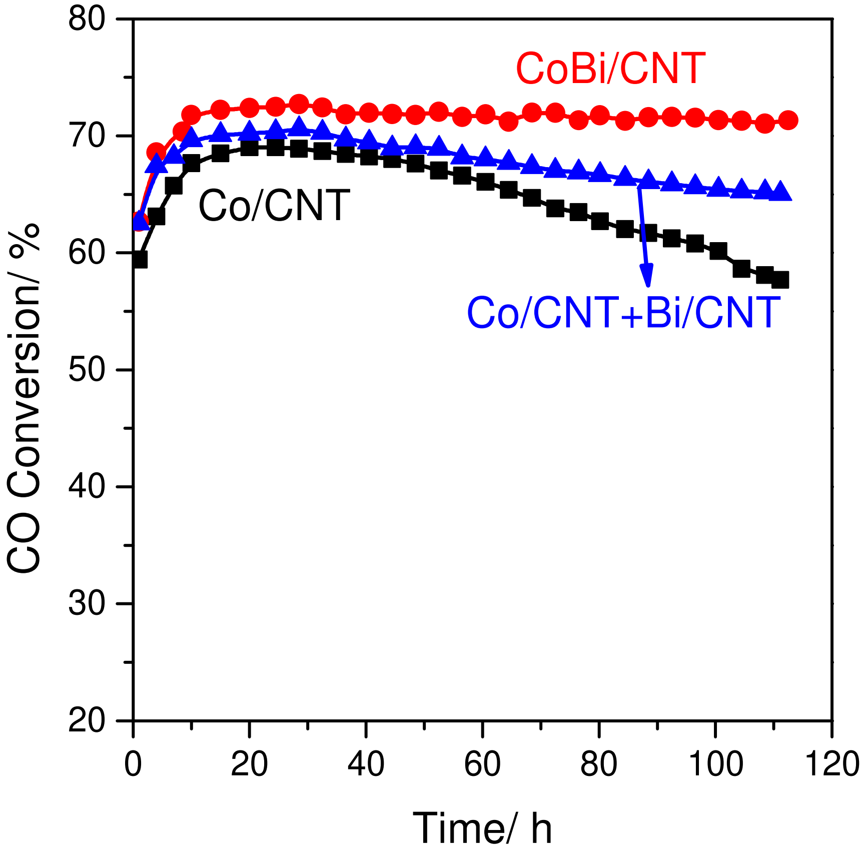

Figure 6. CO conversion versus reaction time during FT synthesis over freshly reduced CNT supported Co catalysts. Reaction condition: 20 bar, H_2/CO=2, GHSV= 6.3 L/g.h, T=250 °C.

In order to accelerate the catalyst deactivation, the reaction temperature was set to 250 °C, which is slightly higher than the conventional temperature for low temperature FT synthesis (220 - 240 °C). All three examined catalysts show similar initial CO conversion (**Figure 6**). The non-promoted Co/CNT catalyst exhibits noticeable deactivation; the CO conversion gradually decreases by about 16% during 110 h of reaction from 68% to 57%. Interestingly, the Bi-promoted Co/CNT catalysts show much more stable catalytic performance compared to the non-promoted counterpart.

Table 1. FT catalytic results over cobalt catalysts measured in the laboratory fixed bed reactor. Conditions: 20 bar, H_2/CO=2, GHSV = 6.3 L/g.h, T=250 ℃, 100 h.

Catalysts	CO conv. (%)	CO_2 selectivity (%)	Hydrocarbon selectivity (%)			
			CH_4	$C_{2-4}^{=}$	C_{2-4}^{0}	C_5^{+}
Co/CNT	57.6	0.5	8.4	5.8	3.1	82.7
CoBi/CNT	71.3	3.8	8.8	6.1	3.3	81.8
Co/CNT+Bi/CNT	65.1	2.7	8.5	6.0	3.4	82.1

The CO conversion remains unchanged over CoBi/CNT at around 72% during 110 h. In addition, we found that Co/CNT+ Bi/CNT prepared by mechanical mixing also presented improved stability compared with the non-promoted Co/CNT catalyst. The catalytic results for the CNT-supported cobalt in FT synthesis are consistent with our previous work [11], which reported the enhanced stability of silica supported cobalt catalysts on their promotion with Bi.

Operando Quick-XAS experiments in the capillary operando reactor

In order to provide further insights into the role of bismuth regarding the cobalt reducibility and catalyst stability, we performed *operando* Quick-XAS measurements with the same catalysts in a capillary setup accompanied with the simultaneous measurements of catalytic performance. The procedure is presented below. The catalysts were reduced in hydrogen flow at 400 ºC, the FT reaction was conducted at 250 ºC, $H_2/CO = 2$ and P = 10 bar for 2 h. In another set of experiments, after reduction, the cobalt catalysts were cooled down to 50 °C, purged under nitrogen and passivated in the air flow at the same temperature for 1 h.

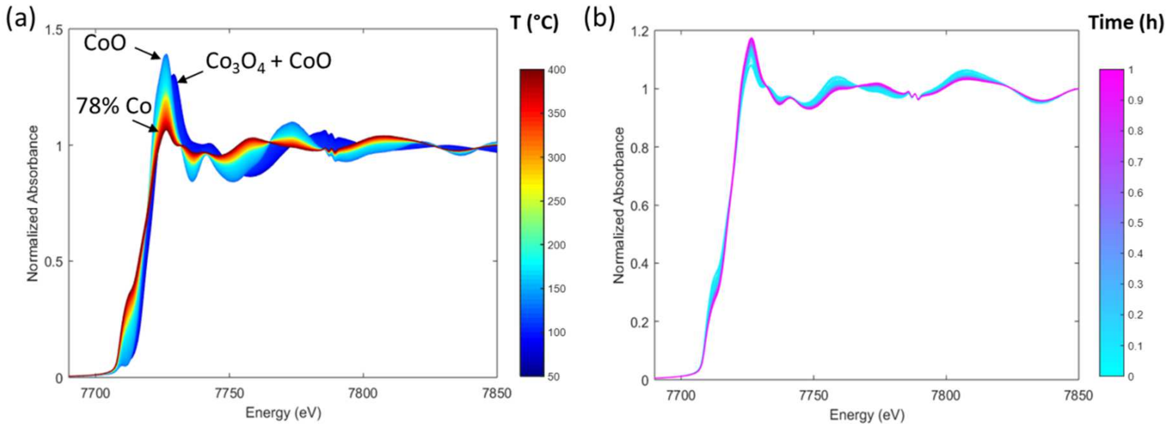

Figure 7. XANES at the K-absorption edge for cobalt phase evolution over Co/CNT catalyst, (a) reduction from 50 ºC to 400 ºC under H_2. (b) the reduced CoBi/CNT was contacted with air at 50 ºC.

Figures 7 and **8** display evolution of the Co K-edge Quick-XAS spectra recorded for the non-promoted Co/CNT and Bi-promoted CoBi/CNT catalysts, respectively. **Figure 9** displays the time evolution of fractions of Co_3O_4, CoO and Co, involved during the reduction and further air passivation for both catalysts determined by MCR-ALS (**Figures S5-S8, SM**).

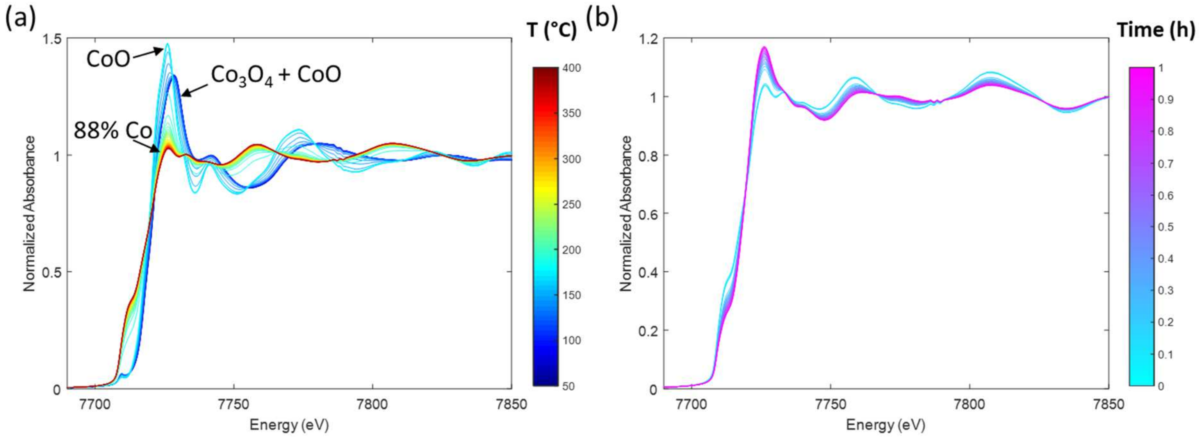

Figure 8. XANES at the K-absorption edge for cobalt phase evolution over CoBi/CNT catalyst, (a) reduction from 50 ºC to 400 ºC under H_2. (b) the reduced Bi was contacted with air at 50 ºC.

In agreement with the XRD results (**Figure 1a**), Quick-XAS detected in the freshly calcined catalysts a mixture of Co_3O_4 and CoO in proportion close to 50:50 (**Figure 9**).

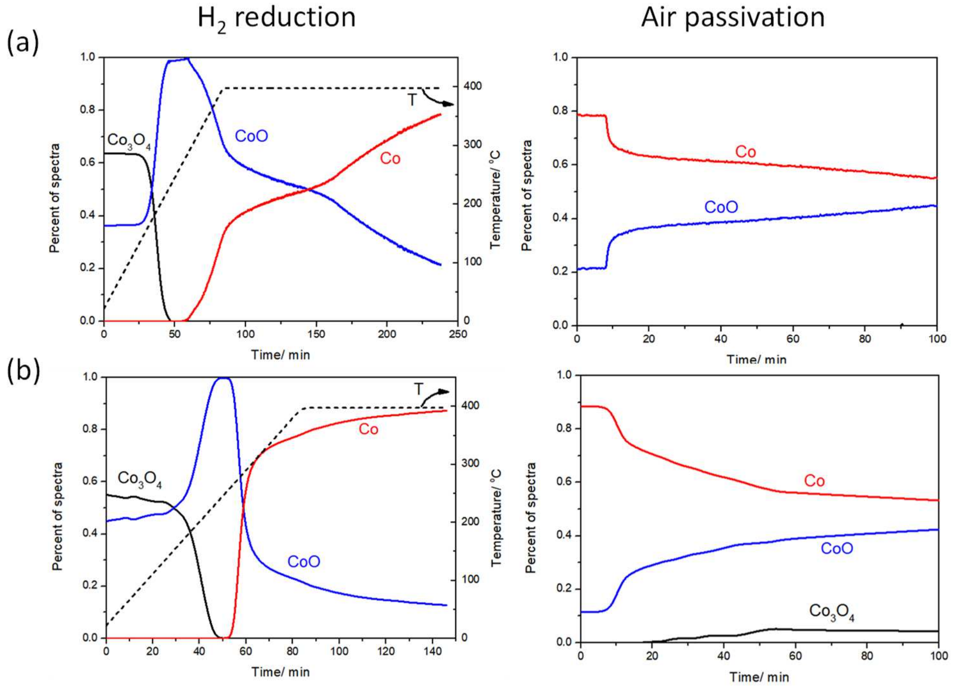

Figure 9. Cobalt speciation determined by MCR-ALS from the Quick-XAS data set recorded for cobalt catalysts during reduction under hydrogen and air oxidation at 50 °C: (a) Co/CNT, (b) CoBi/CNT.

During the hydrogen reduction, the cobalt-based catalysts undergo the reduction from Co_3O_4 to CoO and then to metallic Co (**Figure 7a** and **8a**). The onset of reduction of CoO to Co occurs at 290 °C for the Co/CNT catalyst versus 267 °C for the CoBi/CNT catalyst. In addition to the difference in the temperature of the reduction onset, the cobalt reduction is relatively slow for the Co/CNT catalyst with only 33% of metallic Co formed at the end of the heating ramp under hydrogen against 68% of metallic Co at the same step for the CoBi/CNT catalyst. In order to obtain similar fractions of metallic cobalt after the reduction, a longer time at 400 °C under H_2 has to be used for the unpromoted Co/CNT compared to CoBi/CNT. Namely, nearly the same extent of cobalt reduction can be reached in 60 min at 400 °C for CoBi/CNT with 88 % of metallic Co, while for Co/CNT, it takes 100 min to reach 78 % of metallic Co (**Figure 9**). The speciation determined from the MCR-ALS of the Quick-XAS data is consistent with the TPR data (**Figure 2**). Thus, bismuth acts as a promotor for the cobalt reduction in the catalysts.

The i*n-situ* Quick-XAS spectra at the L_3-edge of Bi (**Figure 10**) show the bismuth phase evolution from oxidic phase to metallic bismuth during hydrogen reduction from 50 ºC to 400 ºC. The impregnated cobalt catalyst is more easily reducible than the catalyst prepared by mechanical mixing. The speciation obtained by MCR-ALS for the CoBi/CNT (**Figure S9-S10, SM**) evidences a direct transformation of the oxidic bismuth species into metallic bismuth, with an onset of reduction at 235 °C and a complete reduction at the end of the heating ramp (**Figure 10c**). The same behavior is reported for the reduction of cobalt for the Co/CNT+ Bi/CNT catalyst than for the

CoBi/CNT with a reduction temperature lower than for the Co/CNT. It is noteworthy that the XANES spectrum of the oxidic bismuth species for the freshly calcined CoBi/CNT is different to those recorded for the Bi_2O_3 reference or for the freshly calcined Bi/CNT catalyst (**Figure S11, SM**). This strongly suggests that the local order around Bi of the CoBi/CNT catalyst is impacted by the presence of cobalt and could indicate the localization of a thin bismuth layer over the surface of cobalt nanoparticles.

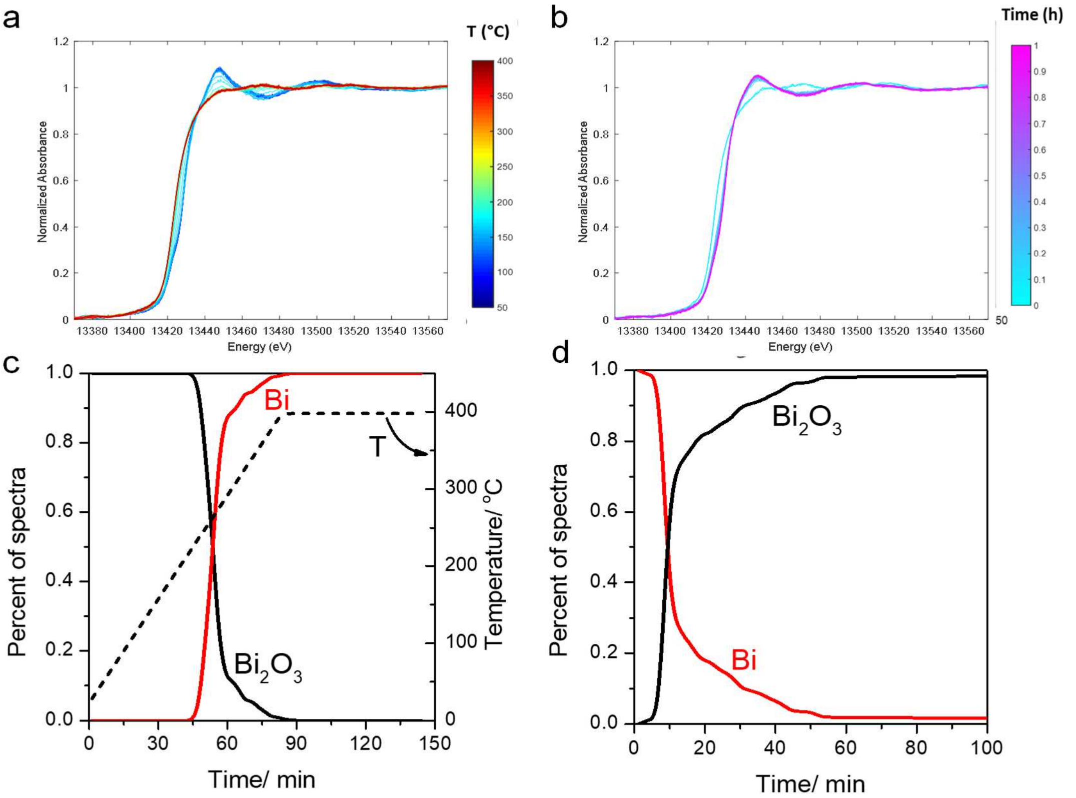

Figure 10. X-ray absorption spectra at the L_3-absorption edge for bismuth phase evolution over CoBi/CNT catalyst, (a) reduction from 50 °C to 400 °C under H_2. (b) reduced CoBi/CNT was contacted with air at 50 °C, (c) Bismuth speciation determined by MCR-ALS from the Quick-XAS data set recorded for the CoBi/CNT catalyst during (c) H_2 activation and (d) air passivation.

After activation under H_2, the Fourier Transforms of the EXAFS spectra of the CoBi/CNT and Bi/CNT catalysts display very different first coordination shell (**Figure S12b, SM**). The fitting of EXAFS Fourier transform moduli for Bi (**Table S2, SM**) at the end of the activation (just before introducing air) of the CoBi/CNT catalyst evidences that Bi is surrounded by 3.8 Co at 2.70 Å. For the fully reduced monometallic Bi/CNT catalyst, Bi has 3 Bi atoms as first neighbors at 3.06 Å and 3 Bi at 3.56 Å. The Bi-Co distance in CoBi/CNT is larger than the Co-Co distance in Co nanoparticles (2.50 Å) but shorter than Bi-Bi in Bi NP, the hypothesis of adsorption of Bi on Co nanoparticles could be an explanation for the presence of Bi-Co coordination. *Operando* EXAFS suggests therefore, that the majority of Bi is in intimate contact with Co.

Table 2. FT catalytic results over cobalt catalysts measured in the in-situ capillary experimental setup at the SOLEIL synchrotron (10 bar, H_2/CO=2, GHSV= 6.3 L/g.h, T=250 ºC, 5 h)

Catalysts	CO conv. (%)	CO_2 selectivity (%)	Hydrocarbon selectivity (%)		
			CH_4	C_2-C_4	C_{5+}
Co/CNT	28.8	0.4	9.8	8.6	81.6
CoBi/CNT	32.6	1.6	10.2	10.5	79.3

The *operando* Quick-XAS data are consistent with the catalytic experiments conducted simultaneously in the capillary reactor (**Table 2**). The initial CO conversions on the Co/CNT and CoBi/CNT catalysts were similar and equal respectively to 28.8% and

32.6%. Higher selectivity to CO_2 has been observed over the Bi-promoted catalysts compared to the monometallic Co/CNT counterpart. Note that the catalytic performance obtained in the *operando* capillary reactor is very similar to that in the laboratory fixed reactor measured under the same conditions (**Table S3, SM**). The *in-situ* Raman spectroscopy also confirmed similar amounts of methane produced on both Co/CNT and CoBi/CNT catalysts during steady step conditions of the FT synthesis in the capillary reactor (**Figure S13, SM**). Note different activation procedures for these catalysts.

In the passivation experiments, after catalyst reduction and exposure to air at 50 °C, XANES at the Co K-absorption edge indicates gradual oxidation of metallic cobalt in both catalysts to cobalt oxides but the transformation rate is 4 times faster for the CoBi/CNT with 0.42 %/min than for the Co/CNT with 0.1 %/min (**Figure 9**). Taking into account that the fraction of metallic cobalt is slightly higher for the CoBi/CNT catalyst (88 %) compared to Co/CNT (78%) before air introduction, a similar fraction of the metallic cobalt phase amounting to 55-56 % is obtained after 60 min of exposure to oxidative atmosphere for the bismuth promoted catalyst and only after 100 min for the unpromoted one. It is noteworthy that more than 70 % of metallic bismuth is oxidized during the first 10 minutes of air exposure (**Figure 10d**) and the remaining metallic bismuth species are fully converted into oxide with a transformation rate of 0.46 %/min. This reduction rate is equivalent to the one reported for cobalt and in agreement with the close vicinity of cobalt and bismuth as deduced from the aforementioned EXAFS fitting. Very fast rate of the oxidation of bismuth in

CoBi/CNT after the catalyst exposure to air compared to cobalt observed by Quick-XAS (**Figures 9** and **10**) is consistent with preferential localization of bismuth in the shell of cobalt nanoparticles.

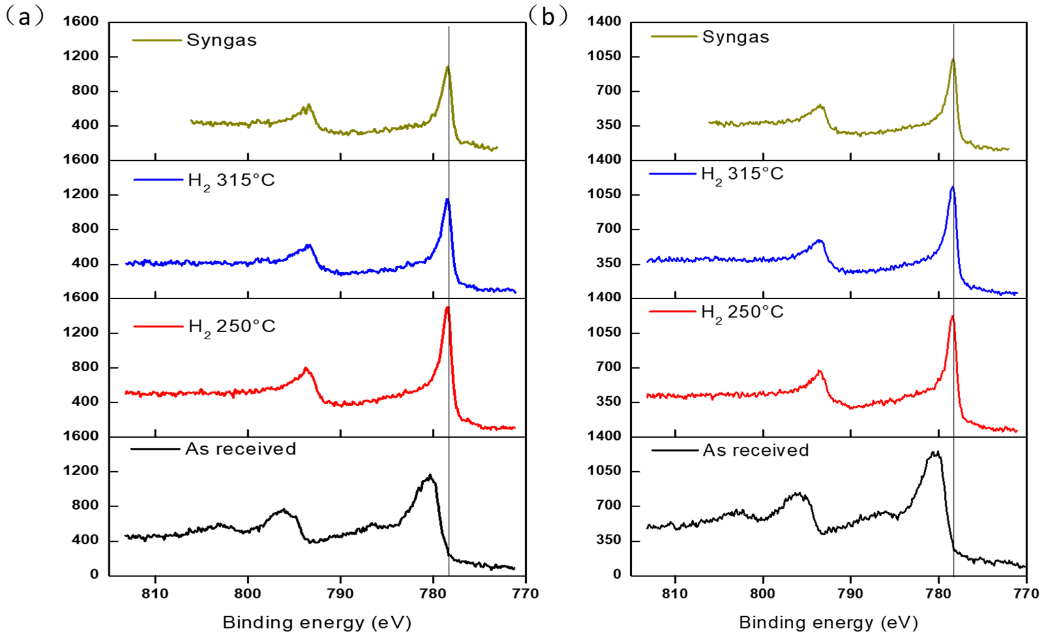

Figure 11. Co 2p NAP-XPS spectra measured in H_2 and syngas at different temperatures: (a) CoBi/CNT; (b) Co/CNT+Bi/CNT .

Evolution of the sub-surface layer in the cobalt catalysts promoted with bismuth in hydrogen and syngas

XPS is one of the most powerful spectroscopic tools to obtain chemical information about the catalyst surface and sub-surface layer. Conventional XPS operates under ultra-high vacuum conditions ($<10^{-8}$ mbar) and is limited to the catalyst characterization before and after catalytic reactions or catalyst pretreatments [37]. NAP-XPS allows the study of the catalyst surface under semi- or pseudo-catalytic conditions at the gas pressures of several millibars at a wide range of temperatures [14,37]. **Figure 11** shows the Co 2p NAP-XPS spectra of the CoBi/CNT and Co/CNT+Bi/CNT catalysts. The spectra of the calcined catalysts are characteristic of the Co_3O_4 phase, which was identified by the binding energy, spin-orbital splitting and low intensity of the satellite peaks [38,39]. The detection of Co_3O_4 by XPS as one of the major cobalt oxide phases in the calcined catalysts is consistent with the XRD and XANES results. Note that in addition to Co_3O_4, XANES and XRD detected a significant fraction (45 %) of cobalt in CoO phase in the oxidized cobalt catalysts. After the temperature increases in H_2 to 250 °C and then to 315 °C, the evolution of the XPS spectra suggests reduction of cobalt oxides to the metallic phase, as identified by the binding energy at ~778 eV [40,41]. After the change of the gas from H_2 to syngas ($H_2/CO=2$) and temperature decrease to the FT reaction temperature (250 °C), cobalt still remains in the metallic phase.

Similar Co 2p XPS spectra were observed for the Co/CNT+Bi/CNT catalyst prepared by mechanical mixing (**Figure 11b**). CoBi/CNT and Co/CNT+Bi/CNT seem to contain similar cobalt phases: Co_3O_4 in the fresh calcined catalysts and mostly cobalt metal phase in the reduced counterparts. The ratios of XPS intensities are shown in **Table 3**.

Table 3. Ratio of corrected[a] XPS intensities measured in the presence of hydrogen and syngas in the NAP-XPS experiments

Catalyst	Gas	Temperature, °C	A_{Co}/A_C	A_{Bi}/A_C
CoBi/CNT	H_2	50	0.0454	0.0013
		250	0.0272	0.0004
		315	0.0223	0.0020
	$H_2/CO=2$	250	0.0196	0.0016
Co/CNT+Bi/CNT	H_2	50	0.0407	0.0013
		250	0.0258	0.0008
		315	0.0190	0.0007
	$H_2/CO=2$	250	0.0201	0.0006

[a] XPS raw intensities divided by transmission and relative sensitivity factor (RSF)

A noticeable decrease in the relative intensity of the Co 2p peaks was observed after the reduction of both CoBi/CNT and Co/CNT+Bi/CNT in hydrogen and subsequent exposure to syngas. The decrease in the XPS intensities corresponds to the decrease in the cobalt surface concentration and could be caused by cobalt sintering. Another possible explanation could be the formation of cobalt-bismuth structures with cobalt localized in the core and bismuth in the shell. This might result in some decrease in the intensity of cobalt XPS signal. The preferential localization of bismuth in the nanoparticle shell in the reduced catalysts is consistent with the STEM-EDX (**Figure 4**) and Quick-XAS.

The Bi 4f NAP-XPS spectra of the Bi-promoted cobalt catalysts are shown in **Figure 12**. The fresh catalysts exhibit Bi 4f peaks with the binding energies [42–44] of 159.0 eV and 164.2 eV, similar to the values found for Bi_2O_3. The catalyst surface composition from NAP-XPS during different treatment steps in the catalyst is shown in **Table S4, SM**. The catalyst exposure to hydrogen at 250 °C leads to the oxidic species reduction to the metallic state with a characteristic doublet [45,46] having a peak at 156.9 eV. Surprisingly, the intensity of Bi XPS peaks decreases in both CoBi/CNT and Co/CNT+Bi/CNT after catalyst heating in hydrogen at 250 °C. This could be an indication of a major decrease in both bismuth surface and sub-surface concentrations. A similar phenomenon was detected in our previous study [14] for bismuth promoted iron catalysts and could be caused by migration and sintering of very mobile bismuth metallic species produced during the reduction of bismuth oxide.

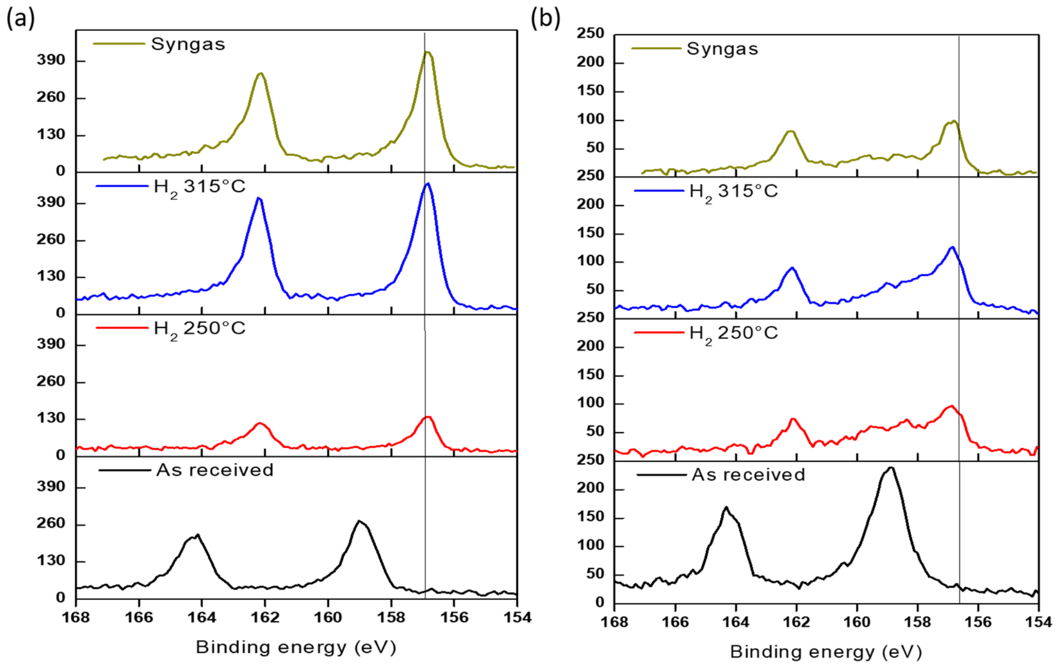

Figure 12. Bi 4f NAP-XPS spectra measured in H_2 and syngas at different temperatures: (a) CoBi/CNT; (b) Co/CNT+Bi/CNT.

At higher reduction temperature (315 °C), the variations of relative intensities (I_{Bi}/I_{C}, **Table 3**) and surface bismuth content (**Table S4, SM**) show different trends for the CoBi/CNT and Co/CNT+Bi/CNT catalysts. Interestingly, the intensity of Bi XPS peaks over the impregnated CoBi/CNT catalyst suddenly increases and gets even higher, while no major modification of intensities of the Bi 4f XPS peaks was observed for Co/CNT+Bi/CNT prepared by mechanical mixing. Indeed, Bi is localized in closer proximity to cobalt in the CoBi/CNT catalyst prepared by impregnation, compared to Co/CNT+Bi/CNT prepared by mechanical mixing. This proximity could facilitate redispersion of bismuth species over cobalt nanoparticles and the formation of cobalt-bismuth core-shell structures. The redispersion of bismuth over cobalt nanoparticles is also consistent with a more significant decrease in the intensity of Co 2p XPS signal in the catalyst prepared by impregnation (**Table 3**) compared to the counterpart prepared by mechanical mixing, where this phenomenon is expected to be less significant.

Table 4. Stability of Bi on different Co surface sites, relative to bulk bismuth oxide, at 227 °C for a H_2/H_2O ratio of 5.

Structure	ΔG_r **(kJ/mol$_{Bi}$)**
Bi(bulk)	31
0.11 ML Bi on Co(111)	-29
0.11 ML Bi on Co(100)	-62
33% Bi on Co(211)	-71

DFT modeling

The thermodynamic stability and preferred localization of Bi on Co catalysts was studied using DFT. **Table 4** provides an overview of the stability of Bi at Co(111) and Co(100) terraces and at Co(211) step sites under FT conditions. While the reduction of Bi_2O_3 to metallic Bi is calculated to be slightly unfavorable under FT conditions (+31 kJ/mol), the calculations show that Bi adsorbs strongly on Co. The formation of CoBi alloys is however, highly unfavorable, with the reaction energy above 350 kJ/mol. Bi binds particularly strongly at the step sites, with a preference of 40 kJ/mol over the Co(111) terrace sites. Lateral interactions between adsorbed Bi atoms are quite weak, and the adsorption energy is constant up to 0.44 ML on the Co(111) terraces (**Figure S14, SM**). Bi is also highly mobile on the Co(111) terraces and along the Co(211) steps, with the diffusion barriers below 20 kJ/mol.

Under FT conditions, CO is the dominant species on Co terraces [47], while both C and CO are the dominant species on the Co step sites [48]. We evaluated the competition between Bi and CO on the Co terraces (**Figures 13** and **S15, SM**).

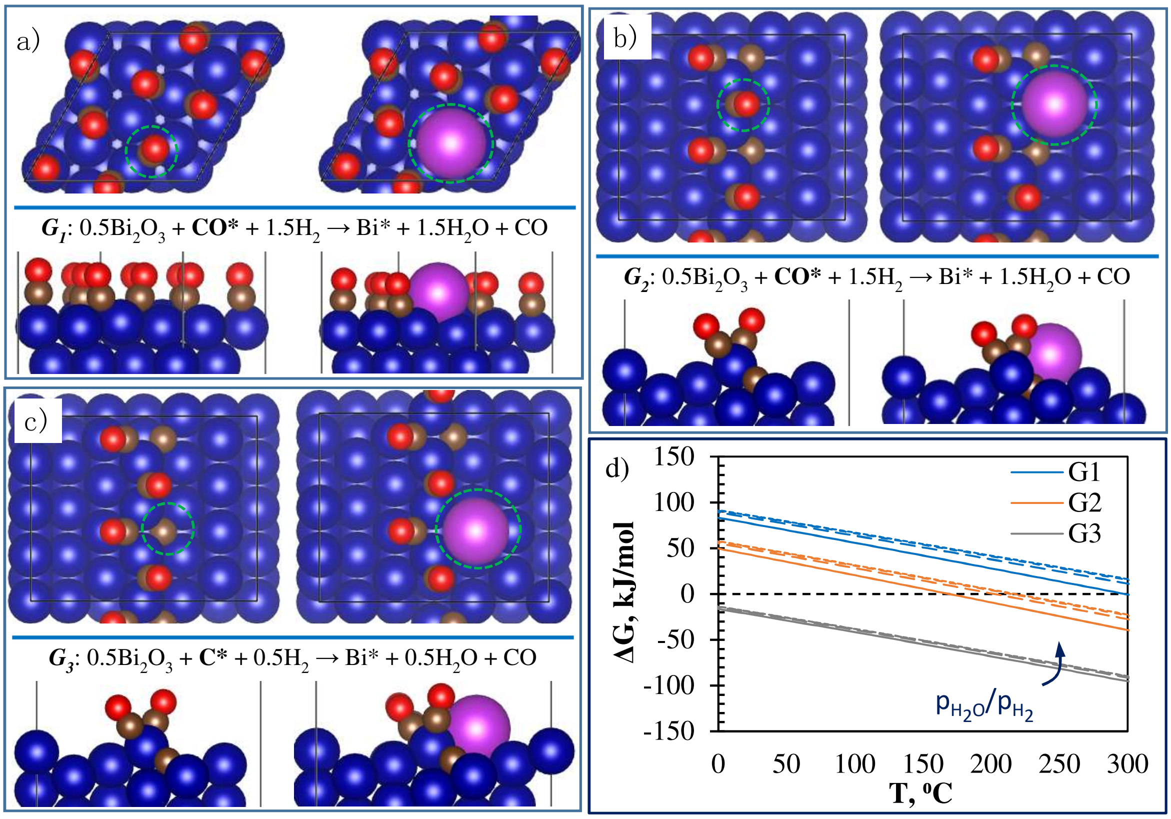

Figure 13. Thermodynamic analysis of the competitive adsorption between (a) Bi and CO* on Co(111) terraces, (b) Bi and CO* at (211) step sites and (c) Bi and C* at Co(211) step sites. (d) Reaction Gibbs free energy for the displacement of CO* and C* by Bi at FT conditions (6.7 bar CO, 13 bar H_2, and H_2/H_2O ratio of 1 – 10.7). More details can be found in **Figure S15, SI**.

Under FT conditions, the CO saturation coverage on the Co terraces is 7/12 ML. Our calculations indicate that at 227 °C, CO is slightly preferred over Bi, and hence, Bi cannot displace CO from the Co terraces (Reaction G1 in **Figure 13d**). At the step sites, the strong adsorption of Bi displaces some of the carbon atoms (Reaction G3 in **Figure 13d**), and CO adsorption is competitive with Bi (Reaction G2 in **Figure 13d**). This finding partially explains the improved coke resistance of Bi-promoted Co catalysts observed in our previous report [11], since coke nucleates at the step sites and hence requires high carbon step concentrations [49]. Bismuth preferentially occupies these sites and thus, suppresses carbon adsorption on the steps.

The strong preference of Bi for the step sites can also explain the observed enhanced sintering resistance [11]. Sintering originates from the migration of undercoordinated Co atoms [50], and the strong adsorption of Bi on the defect sites reduces their surface energy. Previously we showed [51] that extended graphene island and surface carbide were initiated and grown from the step sites. Carbon atoms can diffuse into the step sites to form the p4g surface carbide or grow out of the steps to form graphene strips. The preferential localization of bismuth on the step and edges of cobalt nanoparticles can therefore slows down carbon deposition.

Discussion

Promotion with metals has been a common way to improve the performance of cobalt FT catalysts. Most commonly noble metals (Pt and Ru) have been used. The promotion effects of cobalt FT catalysts due to noble metals have been summarized in recent reviews [5,52]. The present work features a new strategy to improve the performance of cobalt FT catalysts using mobile metal promoters such as bismuth.

In the present work, we showed that the promotion with Bi primarily resulted in better catalyst stability (**Figure 6**), which derives from decreased carbon deposition and cobalt sintering. No catalyst deactivation was observed for the bismuth promoted catalysts prepared by impregnation, while the unpromoted counterpart lost about 20% of the initial activity. Bismuth promotion has no effect on the long-chain hydrocarbon selectivity and the promoted catalyst shows similar C_{5+} selectivity compared with the un-promoted cobalt catalyst (**Table 1**). The promotion with bismuth did not lead to any major increase or decrease in FT reaction rate, and any major modification of hydrocarbon selectivity. DFT modeling suggests that CO can displace Bi atoms in the samples with lower Bi content. This may explain still higher catalytic activity of cobalt catalysts with Bi, even when Bi atoms block a high fraction of cobalt active sites. The bismuth promoted catalyst shows somewhat higher selectivity to CO_2 (**Tables 1, 2** and **S3, SM**). In previous work [11], we uncovered that bismuth promotion facilitated removal of carbon species from cobalt via a combination of CO hydrogenation and carbon oxidation :

$C_{coke} + 2CO + 4H_2 = CO_2 + 2CH_4$, $\Delta G = -142.0$ kJ/mol (250°C)

This could explain the reduced carbon deposition on the Bi promoted cobalt catalysts and their better stability. According to the reaction shown above, the methane yield should twice higher than the amount of CO_2 produced. Another reason contributing to higher CO_2 selectivity could be reaction of CO with adsorbed oxygen over bismuth-promoted cobalt catalysts. Previously, we have observed [53] this effect over iron catalysts promoted with Bi.

The bismuth-promoted cobalt catalysts exhibit better stability in FT synthesis. A combination of techniques suggests that the promotion of CNT-supported cobalt catalysts with bismuth mobile promoter results in a strong interaction of cobalt with the promoter. First, we found using TPR (**Figure 2**) and *in-situ* Quick-XAS (**Figure 9**) that bismuth facilitates the reduction of cobalt species in the supported FT catalysts. The promotion of cobalt catalysts with bismuth results in a higher extent of cobalt reduction after the same duration of catalyst exposure to hydrogen. Our *operando* Quick-XAS data (**Figure 9**) are indicative of a much higher fraction of metallic cobalt in the bismuth promoted catalysts after 60 min of isothermal reduction at 400 °C than for the unpromoted one and much quicker cobalt reduction after passivation in air.

Metallic bismuth has a relatively low melting point and extremely high mobility during the catalyst activation. Using a combination of methods (STEM-EDX, *operando* Quick-XAS, NAP-XPS), we observed migration of bismuth and formation of cobalt bismuth core-shell nanoparticles in the reduced catalysts. Interestingly, NAP-XPS uncovered that migration only occurs, when bismuth gets reduced to the metallic state. First, after the reduction, metallic bismuth forms relatively large liquid droplets and then it gets re-dispersed over cobalt nanoparticles. The NAP-XPS results are consistent with STEM-EDX, which showed a high concentration of cobalt-bismuth core-shell nanoparticles in the reduced catalysts. Passivation under air flow has been used in this work in order to confirm bismuth localization on the surface of cobalt nanoparticles. Selective localization of bismuth in the shell of cobalt nanoparticles is consistent with very fast oxidation of bismuth compared to cobalt during the passivation shown by *operando* Quick-XAS (**Figures 9** and **10d**). Note that the Co-Bi core shell structures may only exist at higher Bi content. The core-shell particles in the sample with 2 wt.% Bi were confirmed by HRTEM and STEM-EDX (**Figures 4 and 5**). At lower Bi content (0.2 wt.%), the amount of bismuth is not sufficient to form a complete shell and, in agreement with DFT modeling bismuth selectively blocks cobalt sites at the steps and edges of cobalt nanoparticles. It is usually considered [54–56] that steps, corners and edges of cobalt nanoparticles may provide active sites for FT synthesis. Bismuth can cover some of these active sites [11]. The catalytic data shows that the CO conversion indeed decreases spectacularly for high Bi contents. At Bi content below 0.2 wt. %, the effect of Bi promotion on the FT reaction rate is not very pronounced, while the catalyst stability is remarkably enhanced. Therefore, sufficient step, corner and edge sites remain available for FT reaction in the studied bismuth promoted catalysts.

The enhanced stability of bismuth promoted catalyst against carbon deposition comes from oxidation of the refractory carbon deposits by oxygen species [11] located over bismuth layer generated during dissociation of CO, which coincides with slightly higher CO_2 production during CO hydrogenation (**Tables 1, 2** and **S3, SM**). DFT modeling also suggests easy diffusion of bismuth on Co(111) terraces and along Co(211) steps. Preferential bismuth adsorption over cobalt low coordinated sites decreases the surface energy and stabilizes cobalt nanoparticles against sintering. On the other hand, as it was previously suggested [51], blocking by bismuth of the edge and step sites reduces carbon deposition. By blocking these defect sites and reducing the surface energy, bismuth is expected to improve the nanoparticle stability against sintering at low bismuth content.

Conclusion

A combination of *operando* Quick XAS, NAP-XPS, STEM-EDX; conventional characterization and catalytic experiments allowed elucidation of evolution of the cobalt and bismuth species in the CNT-supported catalysts and reasons of enhanced catalyst stability during FT synthesis. The presence of bismuth in cobalt catalyst facilitates their reduction. After the hydrogen reduction, bismuth atoms migrate over the catalyst surface and interact with cobalt forming core-shell nanoparticles; cobalt is localized in the core, while bismuth atoms are situated in the nanoparticle layer. At low bismuth coverage, DFT modelling suggests preferential localization of bismuth at the steps and edges of cobalt nanoparticles, which may hinder cobalt sintering and carbon deposition.

Acknowledgments

The authors thank Dr Joelle Thibaut, Laurence Burly and Olivier Gardoll for the help with elementary analysis, XRD and TPR. Thanks are due to Dr. E. Marceau for inspiring discussions about metal catalysts. The authors acknowledge financial support from European Union (Interreg V project PSYCHE) and French National Research Agency (Multiprobe project, Ref. ANR-20-CE42-007). T.G.G. is grateful to the Flemish Research Foundation (FWO) under the CATCO2RE project (S004118N) for financial support. The authors acknowledge the CERIC-ERIC Consortium for the access to experimental facilities and financial support. The authors thank the SOLEIL synchrotron for using the beam time. GENESIS is supported by the Région Haute-Normandie, the Métropole Rouen Normandie, the CNRS via LABEX EMC and the French National Research Agency as a part of the Program "Investissements d'avenir" (PIA) with the references ANR-11-EQPX-0020. The ROCK beamline construction and operation, was also funded by a PIA grant with the reference ANR-10-EQPX-0045. Computational resources and services used in this work were provided by the VSC (Flemish Supercomputer Center), funded by the Research Foundation - Flanders (FWO) and the Flemish Government.

Reference

[1] J. Grunes, J. Zhu, G.A. Somorjai, Catalysis and nanoscience, Chem. Commun. (2003) 2257. https://doi.org/10.1039/b305719b.

[2] D. Astruc, F. Lu, J.R. Aranzaes, Nanoparticles as recyclable catalysts: the frontier between homogeneous and heterogeneous catalysis, Angew. Chemie Int. Ed. 44 (2005) 7852–7872. https://doi.org/10.1002/anie.200500766.

[3] J.M. Campelo, D. Luna, R. Luque, J.M. Marinas, A.A. Romero, Sustainable preparation of supported metal nanoparticles and their applications in catalysis, ChemSusChem. 2 (2009) 18–45. https://doi.org/10.1002/cssc.200800227.

[4] C. Gao, F. Lyu, Y. Yin, Encapsulated metal nanoparticles for catalysis, Chem. Rev. (2020). https://doi.org/10.1021/acs.chemrev.0c00237.

[5] A.Y.Khodakov, W. Chu, P. Fongarland, Advances in the development of novel cobalt Fischer-Tropsch catalysts for synthesis of long-chain hydrocarbons and clean fuels, Chem. Rev. 107 (2007) 1692–1744. https://doi.org/10.1021/cr050972v.

[6] W. Zhou, K. Cheng, J. Kang, C. Zhou, V. Subramanian, Q. Zhang, Y. Wang, New horizon in C1 chemistry: Breaking the selectivity limitation in transformation of syngas and hydrogenation of CO_2 into hydrocarbon chemicals and fuels, Chem. Soc. Rev. 48 (2019) 3193–3228. https://doi.org/10.1039/c8cs00502h.

[7] A.Y. Khodakov, Fischer-Tropsch synthesis: Relations between structure of cobalt catalysts and their catalytic performance, Catal. Today. 144 (2009) 251–

257. https://doi.org/10.1016/j.cattod.2008.10.036.

[8] Y. Chen, J. Wei, M.S. Duyar, V. V. Ordomsky, A.Y. Khodakov, J. Liu, Carbon-based catalysts for Fischer–Tropsch synthesis, Chem. Soc. Rev. (2021) 6248–6272. https://doi.org/10.1039/D0CS00905A.

[9] T. Daeneke, K. Khoshmanesh, N. Mahmood, I.A. De Castro, D. Esrafilzadeh, S.J. Barrow, M.D. Dickey, K. Kalantar-Zadeh, Liquid metals: Fundamentals and applications in chemistry, Chem. Soc. Rev. 47 (2018) 4073–4111. https://doi.org/10.1039/c7cs00043j.

[10] G. Bo, L. Ren, X. Xu, Y. Du, S. Dou, Recent progress on liquid metals and their applications, Adv. Phys. X. 3 (2018) 412–442. https://doi.org/10.1080/23746149.2018.1446359.

[11] B. Gu, M. Bahri, O. Ersen, A. Khodakov, V.V.Ordomsky, Self-regeneration of cobalt and nickel catalysts promoted with bismuth for non-deactivating performance in carbon monoxide hydrogenation, ACS Catal. 9 (2019) 991–1000. https://doi.org/10.1021/acscatal.8b03991.

[12] B. Gu, S. He, D.V. Peron, D.R.Strossi Pedrolo, S. Moldovan, M.C. Ribeiro, B. Lobato, P.A.Chernavskii, V.V.Ordomsky, A.Y. Khodakov, Synergy of nanoconfinement and promotion in the design of efficient supported iron catalysts for direct olefin synthesis from syngas, J. Catal. 376 (2019) 1–16. https://doi.org/10.1016/j.jcat.2019.06.035.

[13] B. Gu, V.V. Ordomsky, M. Bahri, O. Ersen, P.A.Chernavskii, D. Filimonov, A.Y.Khodakov, Effects of the promotion with bismuth and lead on direct

synthesis of light olefins from syngas over carbon nanotube supported iron catalysts, Appl. Catal. B Environ. 234 (2018) 153–166. https://doi.org/10.1016/j.apcatb.2018.04.025.

[14] B. Gu, D. V. Peron, A.J. Barrios, M. Bahri, O. Ersen, M. Vorokhta, B. Šmíd, D. Banerjee, M. Virginie, E. Marceau, R. Wojcieszak, V. V. Ordomsky, A.Y. Khodakov, Mobility and versatility of the liquid bismuth promoter in the working iron catalysts for light olefin synthesis from syngas, Chem. Sci. 11 (2020) 6167–6182. https://doi.org/10.1039/d0sc01600d.

[15] J.A. Moulijn, A.E. Van Diepen, F. Kapteijn, Catalyst deactivation: Is it predictable? What to do?, Appl. Catal. A Gen. 212 (2001). https://doi.org/10.1016/S0926-860X(00)00842-5.

[16] B. Gu, C. Zhou, S. He, S. Moldovan, P.A.Chernavskii, V.V.Ordomsky, A.Y. Khodakov, Size and promoter effects on iron nanoparticles confined in carbon nanotubes and their catalytic performance in light olefin synthesis from syngas, Catal. Today. 357 (2020) 203–213. https://doi.org/10.1016/j.cattod.2019.05.054.

[17] V. Briois, C. La Fontaine, S. Belin, L. Barthe, T. Moreno, V. Pinty, A. Carcy, R. Girardot, E. Fonda, ROCK: the new Quick-EXAFS beamline at SOLEIL, J. Phys. Conf. Ser. 712 (2016) 012149. https://doi.org/10.1088/1742-6596/712/1/012149.

[18] E. Fonda, A. Rochet, M. Ribbens, L. Barthe, S. Belin, V. Briois, The SAMBA quick-EXAFS monochromator: XAS with edge jumping, J. Synchrotron

Radiat. 19 (2012) 417–424. https://doi.org/10.1107/S0909049512009703.

[19] C. Lesage, E. Devers, C. Legens, G. Fernandes, O. Roudenko, V. Briois, High pressure cell for edge jumping X-ray absorption spectroscopy: Applications to industrial liquid sulfidation of hydrotreatment catalysts, Catal. Today. 336 (2019) 63–73. https://doi.org/10.1016/j.cattod.2019.01.081.

[20] J. Jaumot, R. Gargallo, A. de Juan, R. Tauler, A graphical user-friendly interface for MCR-ALS: a new tool for multivariate curve resolution in MATLAB, Chemom. Intell. Lab. Syst. 76 (2005) 101–110. https://doi.org/10.1016/j.chemolab.2004.12.007.

[21] J. Jaumot, A. de Juan, R. Tauler, MCR-ALS GUI 2.0: New features and applications, Chemom. Intell. Lab. Syst. 140 (2015) 1–12. https://doi.org/10.1016/j.chemolab.2014.10.003.

[22] J. Hong, E. Marceau, A.Y. Khodakov, L. Gaberová, A. Griboval-Constant, J.-S. Girardon, C. La Fontaine, V. Briois, Speciation of ruthenium as a reduction promoter of silica-supported Co catalysts: a time-resolved in situ xas investigation, ACS Catal. 5 (2015) 1273–1282. https://doi.org/10.1021/cs501799p.

[23] W.H. Cassinelli, L. Martins, A.R. Passos, S.H. Pulcinelli, C. V. Santilli, A. Rochet, V. Briois, Multivariate curve resolution analysis applied to time-resolved synchrotron X-ray Absorption Spectroscopy monitoring of the activation of copper alumina catalyst, Catal. Today. 229 (2014) 114–122. https://doi.org/10.1016/j.cattod.2013.10.077.

[24] B. Ravel, M. Newville, ATHENA, ARTEMIS, HEPHAESTUS: Data analysis for X-ray absorption spectroscopy using IFEFFIT, J. Synchrotron Radiat. 12 (2005) 537–541. https://doi.org/10.1107/S0909049505012719.

[25] A. Rochet, V. Moizan, F. Diehl, C. Pichon, V. Briois, Quick-XAS and Raman operando characterisation of a cobalt alumina-supported catalyst under realistic Fischer–Tropsch reaction conditions, Catal. Today. 205 (2013) 94–100. https://doi.org/10.1016/j.cattod.2012.08.021.

[26] F. (Feng) Tao, Design of an in-house ambient pressure AP-XPS using a bench-top X-ray source and the surface chemistry of ceria under reaction conditions, Chem. Commun. 48 (2012) 3812. https://doi.org/10.1039/c2cc17715c.

[27] K. Lee, É.D. Murray, L. Kong, B.I. Lundqvist, D.C. Langreth, Higher-accuracy van der Waals density functional, Phys. Rev. B. 82 (2010) 081101. https://doi.org/10.1103/PhysRevB.82.081101.

[28] J. Klimeš, D.R. Bowler, A. Michaelides, Van der Waals density functionals applied to solids, Phys. Rev. B. 83 (2011) 195131. https://doi.org/10.1103/PhysRevB.83.195131.

[29] G. Kresse, J. Hafner, Ab initio molecular dynamcis for liquid metals, Phys. Rev. B. 47 (1993) 558.

[30] G. Kresse, J. Hafner, Ab initio molecular dynamics for open-shell transition metals, Phys. Rev. B. 48 (1993) 13115–13118. https://doi.org/10.1103/PhysRevB.48.13115.

[31] E. van Steen, G.S. Sewell, R.A. Makhothe, C. Micklethwaite, H. Manstein, M.

de Lange, C.T. O'Connor, TPR Study on the Preparation of Impregnated Co/SiO$_2$ Catalysts, J. Catal. 162 (1996) 220–229. https://doi.org/10.1006/jcat.1996.0279.

[32] A.Y. Khodakov, J. Lynch, D. Bazin, B. Rebours, N. Zanier, B. Moisson, P. Chaumette, Reducibility of cobalt species in silica-supported Fischer-Tropsch catalysts, J. Catal. 168 (1997) 16–25. https://doi.org/10.1006/jcat.1997.1573.

[33] A.Y. Khodakov, A. Griboval-Constant, R. Bechara, F. Villain, Pore-size control of cobalt dispersion and reducibility in mesoporous silicas, J. Phys. Chem. B. 105 (2001) 9805–9811. https://doi.org/10.1021/jp011989u.

[34] A. Tavasoli, K. Sadagiani, F. Khorashe, A.A. Seifkordi, A.A. Rohani, A. Nakhaeipour, Cobalt supported on carbon nanotubes - A promising novel Fischer-Tropsch synthesis catalyst, Fuel Process. Technol. 89 (2008) 491–498. https://doi.org/10.1016/j.fuproc.2007.09.008.

[35] M. Zaman, A. Khodadi, Y. Mortazavi, Fischer-Tropsch synthesis over cobalt dispersed on carbon nanotubes-based supports and activated carbon, Fuel Process. Technol. 90 (2009) 1214–1219. https://doi.org/10.1016/j.fuproc.2009.05.026.

[36] A. Tavasoli, M. Trépanier, A.K. Dalai, N. Abatzoglou, Effects of confinement in carbon nanotubes on the activity, selectivity, and lifetime of fischer-tropsch co/carbon nanotube catalysts, J. Chem. Eng. Data. 55 (2010) 2757–2763. https://doi.org/10.1021/je900984c.

[37] L. Zhong, D. Chen, S. Zafeiratos, A mini review of in situ near-ambient

pressure XPS studies on non-noble, late transition metal catalysts, Catal. Sci. Technol. 9 (2019) 3851–3867. https://doi.org/10.1039/c9cy00632j.

[38] J.P. Bonnelle, J. Grimblot, A. D'huysser, Influence de la polarisation des liaisons sur les spectres esca des oxydes de cobalt, J. Electron Spectros. Relat. Phenomena. 7 (1975) 151–162. https://doi.org/10.1016/0368-2048(75)80047-8.

[39] T.J. Chuang, C.R. Brundle, D.W. Rice, Interpretation of the x-ray photoemission spectra of cobalt oxides and cobalt oxide surfaces, Surf. Sci. 59 (1976) 413–429. https://doi.org/10.1016/0039-6028(76)90026-1.

[40] D.G. Castner, P.R. Watson, I.Y. Chan, X-ray absorption spectroscopy, x-ray photoelectron spectroscopy, and analytical electron microscopy studies of cobalt catalysts. 2. Hydrogen reduction properties, J. Phys. Chem. 94 (1990) 819–828. https://doi.org/10.1021/j100365a057.

[41] C.R. Brundle, T.J. Chuang, D.W. Rice, X- ray photoemission study of the interaction of oxygen and air with clean cobalt surfaces, Surf. Sci. 60 (1976) 286–300. https://doi.org/10.1016/0039-6028(76)90318-6.

[42] H. Fan, L. Hu, K. Yang, Y. Fang, Structure and physical properties of Bi_2O_3–B_2O_3–Ga_2O_3 glasses, J. Non. Cryst. Solids. 356 (2010) 1814–1818. https://doi.org/10.1016/j.jnoncrysol.2010.07.011.

[43] B. Oprea, T. Radu, S. Simon, XPS investigation of atomic environment changes on surface of B2O3–Bi2O3 glasses, J. Non. Cryst. Solids. 379 (2013) 35–39. https://doi.org/10.1016/j.jnoncrysol.2013.07.024.

[44] V.S. Dharmadhikari, S.R. Sainkar, S. Badrinarayan, A. Goswami,

Characterisation of thin films of bismuth oxide by X-ray photoelectron spectroscopy, J. Electron Spectros. Relat. Phenomena. 25 (1982) 181–189. https://doi.org/10.1016/0368-2048(82)85016-0.

[45] L. Escobar-Alarcón, J.G. Morales-Mendez, D.A. Solís-Casados, S. Romero, M. Fernández, E. Haro-Poniatowski, Preparation and characterization of bismuth nanostructures deposited by pulsed laser ablation, J. Phys. Conf. Ser. 582 (2015). https://doi.org/10.1088/1742-6596/582/1/012013.

[46] W.E. Morgan, W.J. Stec, J.R. Van Wazer, Inner-Orbital Binding-Energy Shifts of Antimony and Bismuth Compounds, Inorg. Chem. 12 (1973) 953–955. https://doi.org/10.1021/ic50122a054.

[47] G.T.K.K. Gunasooriya, A.P. Van Bavel, H.P.C.E. Kuipers, M. Saeys, CO adsorption on cobalt: Prediction of stable surface phases, Surf. Sci. 642 (2015) L6–L10. https://doi.org/10.1016/j.susc.2015.06.024.

[48] A. Banerjee, V. Navarro, J.W.M. Frenken, A.P. Van Bavel, H.P.C.E. Kuipers, M. Saeys, Shape and Size of Cobalt Nanoislands Formed Spontaneously on Cobalt Terraces during Fischer-Tropsch Synthesis, J. Phys. Chem. Lett. 7 (2016) 1996–2001. https://doi.org/10.1021/acs.jpclett.6b00555.

[49] K. Fei Tan, J. Xu, J. Chang, A. Borgna, M. Saeys, Carbon deposition on Co catalysts during Fischer–Tropsch synthesis: A computational and experimental study, J. Catal. 274 (2010) 121–129. https://doi.org/10.1016/j.jcat.2010.06.008.

[50] D. Moodley, M. Claeys, E. van Steen, P. van Helden, D. Kistamurthy, K.J. Weststrate, H. Niemantsverdriet, A. Saib, W. Erasmus, J. van de Loosdrecht,

Sintering of cobalt during FTS: Insights from industrial and model systems, Catal. Today. 342 (2020) 59–70. https://doi.org/10.1016/j.cattod.2019.03.059.

[51] K. Fei Tan, J. Xu, J. Chang, A. Borgna, M. Saeys, Carbon deposition on Co catalysts during Fischer-Tropsch synthesis: A computational and experimental study, (2010). https://doi.org/10.1016/j.jcat.2010.06.008.

[52] F. Diehl, A.Y. Khodakov, Promotion of Cobalt Fischer-Tropsch catalysts with noble metals: A review, Oil Gas Sci. Technol. 64 (2009) 11–24. https://doi.org/10.2516/ogst:2008040.

[53] V.V. Ordomsky, Y. Luo, B. Gu, A. Carvalho, P.A. Chernavskii, K. Cheng, A.Y. Khodakov, Soldering of iron catalysts for direct synthesis of light olefins from syngas under mild reaction conditions, ACS Catal. 7 (2017) 6445–6452. https://doi.org/10.1021/acscatal.7b01307.

[54] R.A. van Santen, M.M. Ghouri, S. Shetty, E.M.H. Hensen, Structure sensitivity of the Fischer–Tropsch reaction; molecular kinetics simulations, Catal. Sci. Technol. 1 (2011) 891. https://doi.org/10.1039/c1cy00118c.

[55] R.A. Van Santen, Complementary Structure Sensitive and Insensitive Catalytic Relationships, Acc. Chem. Res. 42 (2009) 57–66. https://doi.org/10.1021/ar800022m.

[56] J.J.C. Geerlings, J.H. Wilson, G.J. Kramer, H.P.C.E. Kuipers, A. Hoek, H.M. Huisman, Fischer–Tropsch technology — from active site to commercial process, Appl. Catal. A Gen. 186 (1999) 27–40. https://doi.org/10.1016/S0926-860X(99)00162-3.